Colloids and Surfaces A: Physicochem. Eng. Aspects 457 (2014) 169–179

Contents lists available at ScienceDirect

Colloids and Surfaces A: Physicochemical and Engineering Aspects

journal homepage: www.elsevier.com/locate/colsurfa

Coupled effects of hydrodynamic and solution chemistry on long-term nanoparticle transport and deposition in saturated porous media

Salini Sasidharan[a,b], Saeed Torkzaban[a,*], Scott A. Bradford[c], Peter J. Dillon[a], Peter G. Cook[a,b]

[a] CSIRO Water for a Healthy Country Flagship Program and CSIRO Land and Water, Glen Osmond, SA 5064, Australia
[b] National Centre for Groundwater Research and Training, Flinders University, Adelaide, SA 5001, Australia
[c] USDA, ARS, Salinity Laboratory, Riverside, CA 92507, United States

HIGHLIGHTS

- The breakthrough curves of the NPs exhibited a bimodal shape with increasing solution ionic strength.
- Deposition dynamics of the NPs was simulated using a two-site kinetic model.
- NP deposition is controlled by the coupled effects of flow velocity, solution chemistry, and particle size.
- NP interactions with the collector tend to strengthen with increasing contact time.

GRAPHICAL ABSTRACT

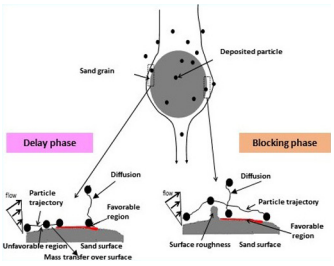

ARTICLE INFO

Article history:
Received 17 March 2014
Received in revised form 28 May 2014
Accepted 29 May 2014
Available online 5 June 2014

Keywords:
Breakthrough curves
Nanoparticle
Column studies
Hydrodynamic
Solution chemistry
Two-site kinetic model

ABSTRACT

This study aims to systematically explore the coupled effects of hydrodynamic and solution chemistry conditions on the long-term transport and deposition kinetics of nanoparticles (NPs) in saturated porous media. Column transport experiments were carried out at various solution ionic strengths (IS), ionic composition, and flow velocities utilizing negatively charged carboxyl-modified latex NPs of two different sizes (50 and 100 nm). These experiments were designed to obtain the long-term breakthrough curves (BTCs) in order to unambiguously determine the full deposition kinetics and the fraction of the solid surface area (S_f) that was available for NP deposition. The BTCs exhibited a bimodal shape with increasing solution IS; i.e., BTCs were initially delayed, next they rapidly increased, and then they slowly approached the influent particle concentration. NP deposition was much more pronounced in the presence of Ca^{2+} than Na^{+} at any given solution IS. Deposition kinetic of NPs was successfully simulated using a two-site kinetic model that accounted for irreversible deposition and blocking on each site, i.e., a decreasing deposition rate as the site filled. Results showed that S_f values were controlled by the coupled effects of flow velocity, solution chemistry, and particle size. Data analyses further demonstrated that only a small fraction of sand surface area contributed in NP deposition even at the highest IS (60 mM) and lowest flow velocity (1 m/day) tested. Consistent with previous studies, our results imply that NP deposition is controlled by physicochemical interactions between the NPs and nanoscale physical and/or chemical heterogeneities on the sand surfaces that produce localized nanoscale favorable sites for deposition. Furthermore, our results suggest that the NP interactions with the collector surfaces tended to strengthen with increasing contact time.

* Corresponding author. Tel.: +61 883038491.
E-mail address: Saeed.Torkzaban@csiro.au (S. Torkzaban).

http://dx.doi.org/10.1016/j.colsurfa.2014.05.075
0927-7757/

1. Introduction

An understanding of nanoparticle (NP) transport and deposition in porous media is important in a range of processes in natural and engineered systems. These processes may include the transport and fate of pathogenic viruses and engineered NPs in soils and aquifers [1–4], and deep bed filtration in water and wastewater treatment systems [5,6]. Most experimental studies of NP deposition in porous media have focused on the initial, clean-bed, deposition behavior when the collector surfaces are devoid or only contain small amounts of deposited particles [4,7,8]. In this case, the deposition rate is constant and a first-order kinetic model is commonly employed to describe the deposition behavior [9,10]. However, as NP deposition on collector surfaces proceeds, a decrease in the deposition rate occurs due to blocking (filling) of the available sites [3,11–14]. This blocking phenomenon usually occurs when a considerable net-repulsive energy barrier exists between the NPs and collector surfaces. Therefore, in most natural systems only a small fraction of the solid surface contributes to NP deposition because of the prevalence of net-repulsive electrostatic conditions [3,15–18]. Consequently, it is imperative that theoretical models are able to describe the entire dynamics of deposition from the initial to later stages when a decline in deposition rates occurs. An understanding of the dynamics of NP deposition is especially important because NP deposition is essentially irreversible (insignificant detachment) during steady-state chemical and hydrodynamic conditions [3,19–22].

Two different blocking models have been developed to describe the declining rate of deposition during the filling process, namely: the Langmuirian model [23,24] and the random sequential adsorption (RSA) model [25,26]. The Langmuirian and RSA models assume a linear and a nonlinear decrease in the deposition rate during filling of deposition sites, respectively. The Langmuirian approach is commonly employed in short-term colloid deposition modeling studies [2,22]. However, the RSA model provides a superior description of deposition dynamics when the coverage of collector surfaces approaches the maximum attainable coverage (~54%), often referred to as the hard sphere jamming limit [24,27–29]. Both Langmuirian and RSA models assume that deposited NPs eventually achieve monolayer coverage on the fraction of the solid surface area that is favorable for deposition (S_f).

Previous studies have reported that S_f is influenced by a range of physicochemical factors such as particle size, the amount and size of physical and/or chemical heterogeneities, solution chemistry, and flow rate [11,30–32]. In particular, S_f has been reported to increase with increasing ionic strength (IS) under net-repulsive electrostatic conditions, suggesting that deposition locations on the collector surfaces are largely determined by nano-scale heterogeneities and/or increasing the depth of the secondary energy minimum [33–36]. Furthermore, increasing the flow velocity and/or particle size has been shown to decrease S_f, suggesting that hydrodynamic conditions are also important in determining deposition kinetics and blocking [2,37,38]. Several explanations have been proposed in the literature to explain the role of flow velocity or particle size on the deposition behavior. Some researchers have attributed the decrease in S_f at higher velocities to the "shadow effect" [37], e.g., the excluded region created down gradient of micro-scale surface roughness or deposited particles. More recently, the influence of hydrodynamic conditions on S_f has been explained by the balance of applied hydrodynamic and resisting adhesive torques [39–43]. Only limited experimental information is available in the literature on the dependence of S_f on physicochemical and hydrodynamic factors, especially for NPs. In this paper, we will systematically explore the coupled effects of these factors on the value of S_f. This information is required to better deduce the underlying mechanisms and theoretical description of NP deposition kinetics under net-unfavorable conditions.

The overall deposition rate of NPs in porous media depends not only on S_f, but also on the mass transfer of NPs to favorable sites on the solid surfaces where deposition can occur. Mass transfer of NPs to favorable sites occurs by two means: (1) aqueous phase mass transfer from the bulk aqueous phase to the solid surface [44,45] and (2) solid phase mass transfer on unfavorable regions of the solid surface to favorable sites [30,33,46]. Aqueous phase mass transfer of NPs to the solid surface has been the subject of much research [10] and colloid filtration theory [47] is commonly used to quantify this process. Conversely, the role of solid phase mass transfer has received less research attention [30]. It has been shown that particles colliding with unfavorable regions of the solid surface may become weakly associated with the solid surface via a shallow secondary energy minimum. These particles can be translated along the collector surface by tangential hydrodynamic forces to favorable deposition sites [48]. It is expected that nano- and micro-scale surface roughness and the pore-space topography should influence the solid phase mass transfer of the NPs. Furthermore, the amount of colloid transfer on the solid surface is expected to increase with increasing IS and decreasing flow velocity [33,35]. The solid phase mass transfer rate of NPs is likely to decrease during the filling processes, but little research has been conducted to address this issue.

The objective of this study is to develop a more thorough understanding of the combined effects of hydrodynamics and solution chemistry on the long-term kinetics of NP deposition in saturated porous media. Specifically, a series of laboratory experiments was carried out in saturated sand columns to investigate the coupled effects of solution IS, cation type, particle size, and flow velocity on the deposition rate constants and the fraction of the sold surface area available for NP deposition. A two-site kinetic model was found to satisfactorily simulate and describe the long-term dynamics of the deposition process. Fitted values of S_f and deposition rate constants over a wide range of physicochemical conditions increased our understanding of the dynamics of long-term NP deposition in porous media. This information is needed to improve our theoretical description of these processes and to improve continuum scale models for predicting the long-term fate and mobility of NPs in the subsurface environment.

2. Materials and methods

2.1. NPs

Carboxylate-modified latex (CML) microspheres have often been used as model NPs in transport studies due to their spherical shape, well-defined size and surface charge, and ease in detection at low concentration [2]. Two sizes (50 and 100 nm) of Fluoresbrite®Yellow-Green CML microspheres (Polysciences, Inc), that have an excitation wavelength at 441 nm and an emission wavelength at 486 nm, were used in this research. Stock solutions of CML NPs were diluted in selected electrolyte solutions to achieve a desired initial concentration (C_0). All solutions were prepared using analytical graded reagents and Milli-Q water with its unadjusted pH 5.8. A near neutral pH and negatively charged NPs were chosen in order to understand the NP transport mechanism under most unfavorable condition. The initial concentration for 50 and 100 nm CML NPs was typically 4.55×10^{10} mL^{-1}. NP aqueous phase concentrations were determined using a fluorescence spectrophotometer (Synergy HT, BioTek Instruments, Inc., Winooski, VT, USA) and a calibration curve. The CML NPs have carboxylate groups on their surfaces that are highly negatively charged. The zeta potential and size uniformity of the CML microspheres in various electrolyte

Table 1
The average of zeta potentials of NPs and sand as well as calculated DLVO interaction parameters in the indicated solution chemistries.

NP size (nm)	Solution chemistry	IS (mM)	Zeta potential (NP) (mV)	Zeta potential (sand) (mV)	Energy barrier height (kT)	Secondary minimum depth (kT)
50	10 mM NaCl	10	−51	−29	57	~0
50	20 mM NaCl	20	−48	−30	52	~0
50	50 mM NaCl	50	−31	−26	24	−0.08
50	0.5 mM $CaCl_2$	1.5	−43	−21	28	~0
50	2 mM CaCl2	6	−32	−19	16	~0
100	40 mM NaCl	40	−41	−15	47	−0.2
100	60 mM NaCl	60	−30	−15	19	−0.3
100	2 mM $CaCl_2$	6	−35	−19	34	~0
100	3 mM $CaCl_2$	9	−27	−17	20	−0.22

and pH solutions were determined using a Malvern, Zetasizer Nano Series, Nano-ZS. It was confirmed that the CML suspension at the highest tested concentrations of 60 mM NaCl and 3 mM $CaCl_2$ was stable and did not show any aggregation. The manufacturer reported that the CML NPs had a density of 1.05 g cm^{-3}.

2.2. Porous media

Natural graded river sand (River sand pty Ltd) was used as the granular porous media for the transport experiments. The average grain diameter of the sand was 255 μm, and the grain size ranged between 106 and 300 μm. The sand was cleaned prior to use to remove the impurities from the sand surface and to reduce the surface heterogeneity. Sieved sand was soaked in 37% HCl for three days to remove dissolved organic matter and metal oxides. After discarding the excess acid, the sand was alternatively rinsed with 0.1 M NaOH and deionized (DI) water until the pH reached 7. The sand was subsequently soaked in boiling 1 M NaCl for 3 h, and then washed with boiling DI water for 3 h. These processes (boiling alternatively in 1 M NaCl and DI water) were repeated eight times to remove the clay particles on the sand surface by the combined influence of cation exchange and expansion of the double layer. Finally the sand was rinsed with DI water several times until the effluent turbidity and UV–visible absorbance was virtually zero. Scanning electron microscopy (SEM) (Quanta 450, Adelaide microscopy, The University of Adelaide, Australia) of the sand before and after cleaning demonstrated that this procedure removed most of the surface impurities and clays from the sand.

2.3. Electrokinetic characterization and DLVO calculations

The electrophoretic mobility of the colloids and crushed sand grains was measured in various NaCl electrolyte solutions at pH 5.8 using a Zetasizer. The Smoluchowski equation [49] was used to convert the measured electrophoretic mobility values to zeta potentials. The measurements were repeated five times for each colloid suspension and the average values are reported in Table 1. Classical DLVO theory [50,51] was used to calculate the total interaction energy, that is, the sum of the London–van der Waals attraction and the electrostatic double-layer repulsion, for the colloids upon close approach to quartz surfaces (assuming sphere–plate interactions) for the various solution IS used in our experiments. The retarded London–van der Waals interaction force was determined from the expression of Gregory [52] utilizing a value of 4.04×10^{-21} J for the Hamaker constant [53] to represent the latex–water–quartz system. In these calculations, constant-potential electrostatic double layer interactions were quantified using the linear superposition approximation model given in Gregory [54], with zeta potentials in place of surface potentials.

2.4. Column studies

Column experiments were conducted using 11 cm long polycarbonate chromatography columns with a 1.9 cm internal diameter and a total inner volume of 31.19 cm^2. Tubing to and from the columns, fittings, and column O-rings were composed of chemically inert material such as Teflon and viton. The columns were set-up vertically and wet packed with the cleaned river sand, using vibration to minimize air entrapment and to ensure the uniformity of packing. A sodium nitrate ($NaNO_3$) tracer test was conducted to obtain the parameter values for the transport modeling. Each column was packed with ~50 g of sand and the porosity was calculated gravimetrically to be 0.40. One pore volume (PV), which is the amount of solution required to fill in the void space of the sand in the column was determined to be 14 mL. The packed columns were flushed with several pore volumes of a selected electrolyte solution to equilibrate the system before injecting a NP suspension at a constant velocity with a syringe pump (Harvard apparatus 22). Effluent samples (every 3 mL) were continuously collected using a Spectra/Chrom® CF-1 Fraction Collector. In order to calculate the amount of surface area that contributed in NP deposition, the injection of the NPs was continued until the effluent concentration (C) approached C_0 or a stable concentration level. The columns were then flushed with several PV of the same electrolyte solution, but without NPs. Table 1 summarizes the experimental conditions. Table 2 contains the number of injected PV at which the influent was switched to the NP-free electrolyte solution.

A few sand grains were collected carefully from the column after the deposition phase. The samples were analyzed using SEM to observe the distribution of NPs on the sand surfaces. Sand grains were placed on the top of a carbon tape mounted on a stub, with a 3 nm thickness platinum coating and imaged at 10 kV using Quanta 450 SEM. It was visually confirmed that the platinum coating force and the vacuum in the SEM chamber were not enough to detach the deposited NPs.

2.5. Modeling

Major processes controlling the transport and deposition of NPs in porous media are advection, dispersion, and attachment caused by particle interactions with the collector surfaces. The detachment process is often negligible under steady-state chemical and hydrodynamic conditions [2] and will be neglected in this work. The advection–dispersion equation (ADE) with irreversible attachment is given for uniform and one-dimensional flow as

$$\frac{\partial C}{\partial t} = \lambda v \frac{\partial^2 C}{\partial z^2} - v \frac{\partial C}{\partial z} - r_{att} \quad (1)$$

where t (T) is time, z (L) is the direction of mean water flow, C (NL^{-3}) is the number of NPs per unit volume of the aqueous phase, λ is the dispersivity (L), v is the average pore water velocity (LT^{-1}), and r_{att} is the NP attachment rate to the solid surfaces ($NL^{-3}T^{-1}$). The mean

Table 2
Experimental conditions and fitted model parameters for column experiments shown in Figs. 1–4.

NP size (nm)	Poe water flow velocity (m/day)	NaCl or $CaCl_2$ (mM)	Pulse duration (PV)	K_1 (min^{-1})	K_2 (min^{-1})	S_{max1}/C_0 (m^3/kg)	S_{max2}/C_0 (m^3/kg)	S_f (fitted)[a] (%)	S_f (BTC)[b] (%)
50	1	10 Na^+	41.5	$(7.3 \pm 0.4) \times 10^{-3}$	$(3.2 \pm 0.6) \times 10^{-3}$	$(4.2 \pm 0.3) \times 10^{-5}$	$(9.8 \pm 0.6) \times 10^{-4}$	0.04	0.03
50	1	20 Na^+	41.2	$(4.8 \pm 0.1) \times 10^{-2}$	$(5.8 \pm 0.3) \times 10^{-3}$	$(1.1 \pm 0.4) \times 10^{-3}$	$(5.4 \pm 0.8) \times 10^{-3}$	0.95	ND[c]
50	1	30 Na^+	35.5	$(1.1 \pm 0.5) \times 10^{-1}$	$(6.4 \pm 0.6) \times 10^{-3}$	$(1.4 \pm 0.2) \times 10^{-3}$	$(7.2 \pm 0.5) \times 10^{-3}$	1.24	ND
50	1	40 Na^+	35.1	$(1.5 \pm 0.4) \times 10^{-1}$	$(7.7 \pm 0.3) \times 10^{-3}$	$(1.6 \pm 0.6) \times 10^{-3}$	$(9.1 \pm 0.7) \times 10^{-3}$	1.46	ND
50	1	50 Na^+	41	$(1.7 \pm 0.5) \times 10^{-1}$	$(1.5 \pm 0.6) \times 10^{-2}$	$(1.7 \pm 0.2) \times 10^{-3}$	$(1.0 \pm 0.5) \times 10^{-2}$	1.78	ND
50	5	50 Na^+	29.7	$(3.7 \pm 0.2) \times 10^{-1}$	$(2.3 \pm 0.3) \times 10^{-2}$	$(1.8 \pm 0.3) \times 10^{-3}$	$(3.6 \pm 0.6) \times 10^{-3}$	1.54	ND
50	20	50 Na^+	38.9	(1.1 ± 0.6)	$(6.9 \pm 0.5) \times 10^{-2}$	$(1.6 \pm 0.4) \times 10^{-3}$	$(2.3 \pm 0.7) \times 10^{-3}$	1.33	ND
100	1	40 Na^+	25.2	$(6.3 \pm 0.3) \times 10^{-3}$	$(4.3 \pm 0.4) \times 10^{-3}$	$(7.8 \pm 0.6) \times 10^{-5}$	$(3.5 \pm 0.2) \times 10^{-4}$	1.45	1.7
100	1	50 Na^+	27.6	$(4.7 \pm 0.2) \times 10^{-2}$	$(2.6 \pm 0.3) \times 10^{-3}$	$(6.5 \pm 0.3) \times 10^{-4}$	$(6.3 \pm 0.7) \times 10^{-4}$	4.32	4.9
100	1	60 Na^+	24.7	$(6.6 \pm 0.5) \times 10^{-2}$	$(2.3 \pm 0.1) \times 10^{-3}$	$(1.2 \pm 0.1) \times 10^{-3}$	$(1.2 \pm 0.3) \times 10^{-3}$	8.16	ND
100	5	50 Na^+	26.8	$(1.1 \pm 0.2) \times 10^{-1}$	$(2.0 \pm 0.2) \times 10^{-2}$	$(2.7 \pm 0.5) \times 10^{-4}$	$(7.9 \pm 0.8) \times 10^{-4}$	2.57	2.3
100	20	50 Na^+	21	$(6.0 \pm 0.4) \times 10^{-2}$	$(4.7 \pm 0.3) \times 10^{-2}$	$(9.7 \pm 0.6) \times 10^{-5}$	$(2.9 \pm 0.3) \times 10^{-4}$	1.30	1.2
50	1	0.5 Ca^{2+}	58.4	$(3.6 \pm 0.2) \times 10^{-2}$	$(3.7 \pm 0.3) \times 10^{-3}$	$(1.4 \pm 0.1) \times 10^{-3}$	$(1.2 \pm 0.2) \times 10^{-2}$	1.29	0.03
50	1	2 Ca^{2+}	83.8	$(5.2 \pm 0.6) \times 10^{-2}$	$(6.0 \pm 0.5) \times 10^{-3}$	$(3.5 \pm 0.4) \times 10^{-3}$	$(4.1 \pm 0.5) \times 10^{-2}$	3.28	ND
50	5	2 Ca^{2+}	57.1	$(1.1 \pm 0.2) \times 10^{-1}$	$(1.7 \pm 0.4) \times 10^{-2}$	$(3.9 \pm 0.2) \times 10^{-3}$	$(1.8 \pm 0.3) \times 10^{-3}$	3.34	ND
50	25	2 Ca^{2+}	14.4	$(1.9 \pm 0.3) \times 10^{-1}$	$(1.7 \pm 0.5) \times 10^{-1}$	$(7.8 \pm 0.6) \times 10^{-5}$	$(6.8 \pm 0.5) \times 10^{-4}$	0.07	0.05
100	1	2 Ca^{2+}	32.5	$(8.2 \pm 0.6) \times 10^{-2}$	$(3.4 \pm 0.2) \times 10^{-3}$	$(1.3 \pm 0.2) \times 10^{-3}$	$(1.6 \pm 0.1) \times 10^{-3}$	4.57	5.3
100	5	2 Ca^{2+}	22.7	$(7.6 \pm 0.5) \times 10^{-2}$	$(6.8 \pm 0.7) \times 10^{-3}$	$(2.3 \pm 0.3) \times 10^{-4}$	$(4.7 \pm 0.6) \times 10^{-4}$	0.79	0.62
100	1	3 Ca^{2+}	33.1	$(1.2 \pm 0.1) \times 10^{-1}$	$(2.7 \pm 0.2) \times 10^{-3}$	$(2.5 \pm 0.2) \times 10^{-3}$	$(3.3 \pm 0.5) \times 10^{-3}$	8.51	ND

[a] Determined by the sum of fitted values of S_{max1} and S_{max2} and using Eq. (4).
[b] Determined from a mass balance calculation of the BTCs and using Eq. (5).
[c] Not determined.

pore-water velocity and dispersivity used in NP simulations were obtained by fitting to the tracer ($NaNO_3$) BTCs.

Typically, the BTCs could be simulated reasonably well during the first few PV using Eq. (1) in conjunction with a one-site, irreversible attachment model that included a Langmurian blocking function. However, as it will be discussed later, this model does not provide an adequate description of the deposition dynamics at later times. To investigate whether multiple kinetic deposition sites could account for this discrepancy, a two-site kinetic model was used for analyzing the BTCs. In this case, the value of r_{att} is given as

$$r_{att} = \rho_b \frac{\partial(S_1 + S_2)}{\partial t} = \theta k_1 \psi_1 C + \theta k_2 \psi_2 C \tag{2}$$

where ρ_b is the soil bulk density (ML^{-3}), θ is the water content, S_1 is the solid phase NP concentration on site 1(NM^{-1}), k_1 is the attachment rate coefficient for site 1 (T^{-1}), and Ψ_1 is a dimensionless Langmuirian blocking function for site 1 that is given as [23]

$$\Psi_1 = \left(1 - \frac{S_1}{S_{max\,1}}\right) \tag{3}$$

Here S_{max1} (NM^{-1}) is the maximum solid phase concentration of attached NPs on site 1. Corresponding values of S_2, S_{max2}, k_2, and Ψ_2 are defined for site 2. When the value of S_{max1} and S_{max2} are large, the blocking function approaches a value of 1 and time-dependent deposition behavior becomes irrelevant. A modified version of HYDRUS-1D [55] was used to solve Eqs. (1)–(3).

The fraction of the solid surface area that is available for deposition (S_f) may be determined from the sum of fitted values of S_{max1} and S_{max2} using the following equation [56]:

$$S_f = \frac{A_c \rho_b S_{max}}{(1-\gamma)A_s} \tag{4}$$

where A_c ($L^2\,N^{-1}$) is the cross section area per colloid, A_s (L^{-1}) is the solid surface area per unit volume, S_{max} (NM^{-1}) is the maximum solid phase concentration of attached NPs on both sites, and γ is the porosity of a monolayer packing of colloids on the solid surface. In this work we assume a value of $\gamma = 0.5$ in all simulations based on information presented by Johnson and Elimelech [25]. For those experiments where C/C_0 reached unity during the deposition phase, the value of S_f can also be estimated from the effluent BTCs based on the following mass balance equation [37]:

$$S_f = \frac{\pi r_p^2 r_c q_w (C_o T_{pulse} \int_0^{T_{total}} C\,dt)}{3L(1-n)} \tag{5}$$

where r_p (L) is the radius of the NP, r_c (L) is the radius of the sand grain, q_w (LT^{-1}) is the Darcy velocity, T_{pulse} (T) is the injection time, and T_{total} (T) is the entire time of the experiment, L (L) is the length of the packed column and n is the porosity of the porous media. As it will be shown later in the paper, Eqs. (4) and (5) were found to yield comparable values of S_f.

3. Results and discussion

3.1. Surface charge of NPs and sand grains

Zeta potentials of the NPs and colloidal particles collected from crushed sand grains over the range of solution chemistries used in the column experiments are presented in Table 1. As expected, the absolute value of the zeta potential of the NPs and sand grains decreased with increasing the concentration of Na^+ and Ca^{2+} due to compression of the electrostatic double layer [49]. Increasing the Ca^{2+} concentration was more effective in decreasing the magnitude of zeta potential than similar changes in Na^+ due to the combined effects of charge screening of the divalent cations and

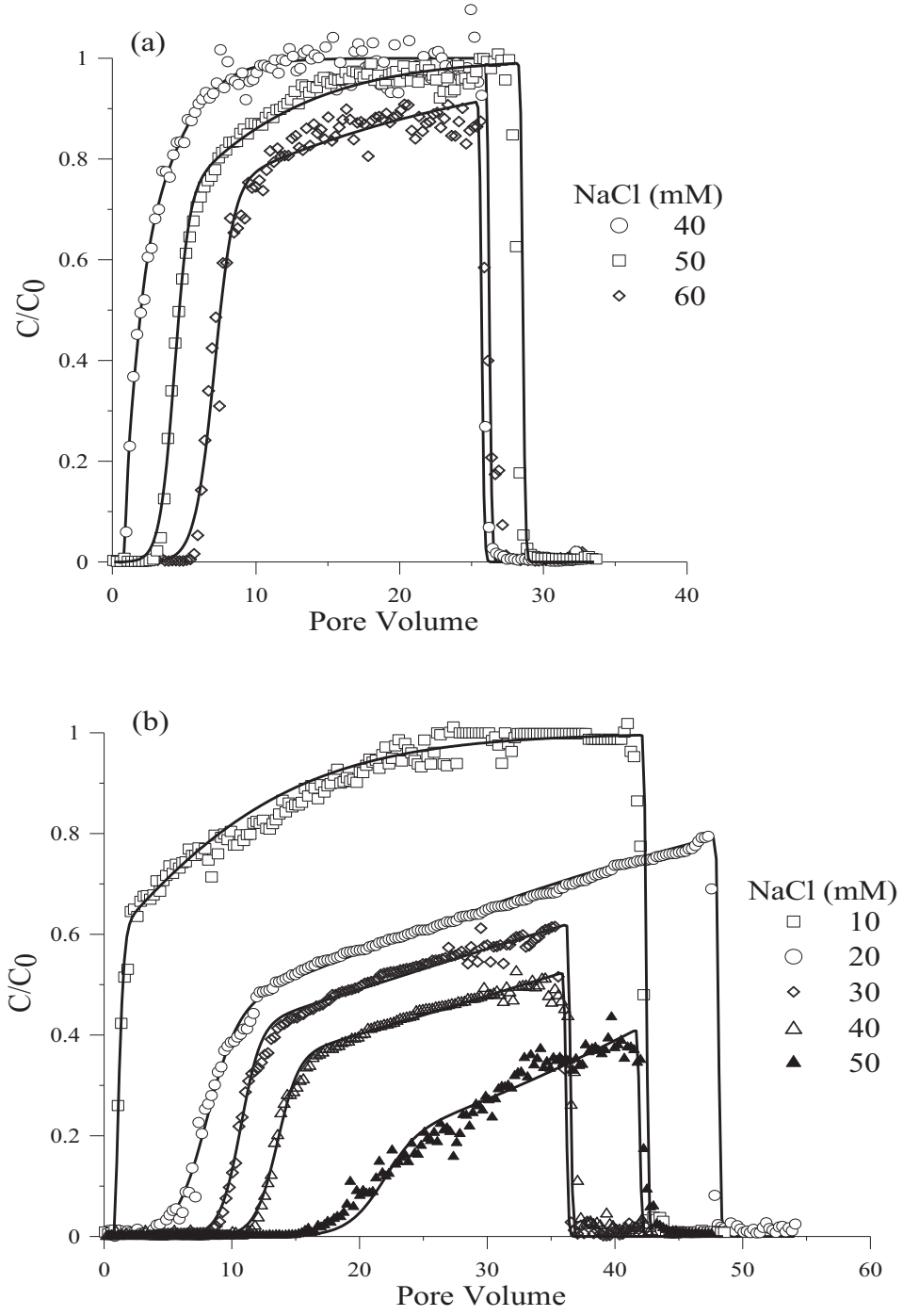

Fig. 1. Representative measured and fitted breakthrough curves for 100 nm (a) and 50 nm (b) modified latex nano-particles obtained from column experiments at pore water velocity of 1 m/day at various NaCl concentrations. Table 2 provides summary information on the model parameters.

the adsorption (binding) of cationic Ca^{2+} to anionic COO^{-} groups on the NPs and SiO_2 sites on the collectors [57].

Calculated DLVO interaction energies presented in Table 1 indicate a negligible secondary energy minimum in all solutions for both of the particle sizes. Therefore, the NPs are expected to experience negligible deposition or aggregation due to the secondary energy minimum. DLVO calculations show high energy barriers (16–52 kT) between the NPs and sand surfaces at all of the considered solution chemistries. The height of energy barriers decreased with IS and decreasing NP size. The Maxwellian kinetic energy model [21,58] predicts that it is unlikely for the NPs to diffuse over these energy barriers into the primary energy minimum. Higher energy barriers and negligible secondary minima suggest that net repulsive interactions should have existed between the NPs and sand grains. However, it should be noted that these interaction energies only reflect mean values of interaction energies between the NPs and sand surfaces and do not account for the potential influence of nano-scale chemical and physical heterogeneities which always exist on natural mineral surfaces [59,15]. It has been demonstrated that nano-scale roughness on collector and colloid surfaces tends to reduce the magnitude of the interaction energies [15,20].

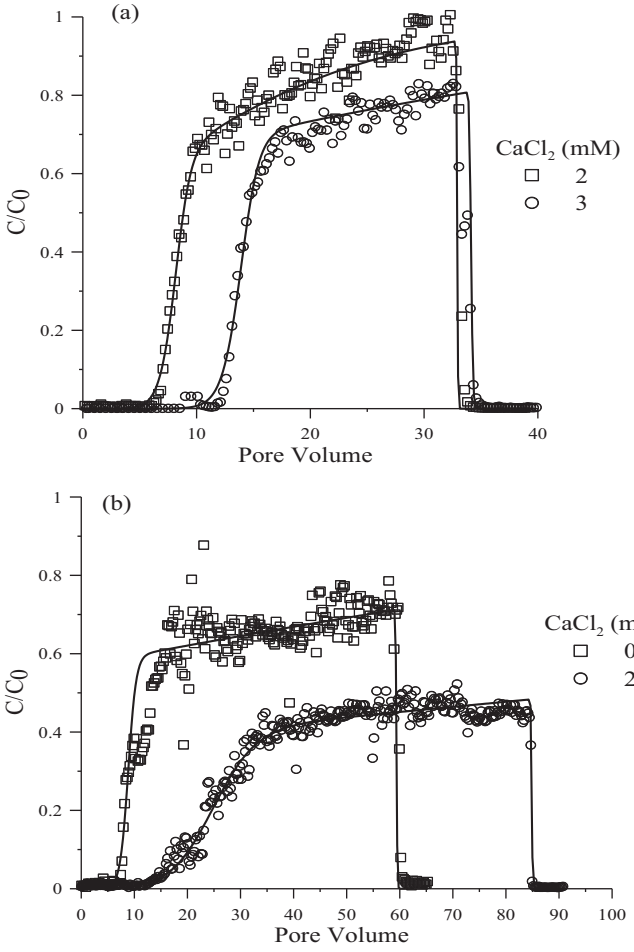

Fig. 2. Representative measured and fitted breakthrough curves for 100 nm (a) and 50 nm (b) modified latex nano-particles obtained from column experiments at pore water velocity of 1 m/day at various $CaCl_2$ concentrations. Table 2 provides summary information on the model parameters.

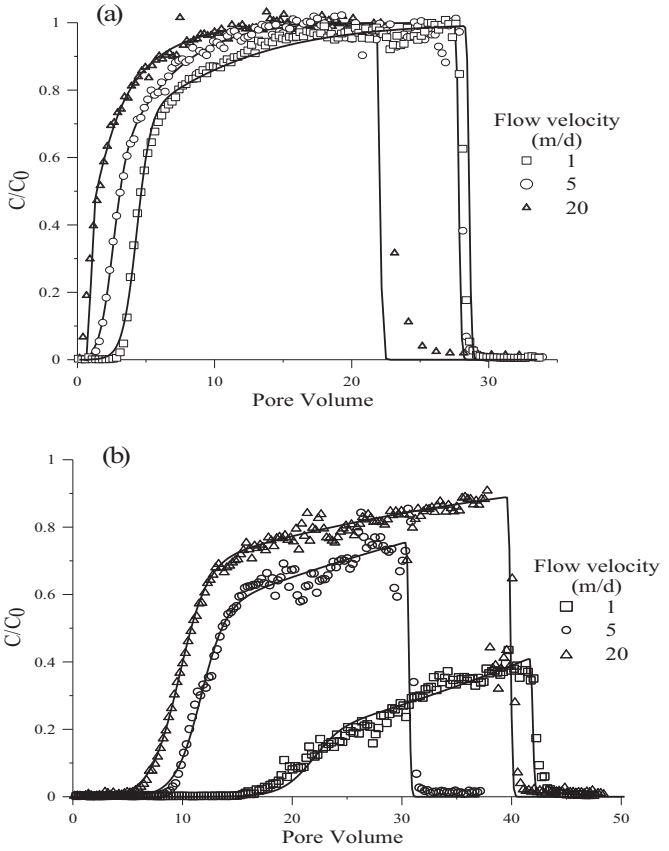

Fig. 3. Representative measured and fitted breakthrough curves for 100 nm (a) and 50 nm (b) modified latex nano-particles obtained from column experiments at 50 mM NaCl and various flow velocities. Table 2 provides summary information on the model parameters.

3.2. Deposition kinetics of NPs

In contrast with most previous studies on NP deposition, reviews of which may be found in [4], long-term injections of the NPs were carried out in order to determine the full dynamics of deposition and the associated blocking model parameters. Fig. 1 presents measured and simulated BTCs for 100 (Fig. 1a) and 50 nm (Fig. 1b) NPs in various concentrations of NaCl solutions when the pore-water velocity was 1 m/day. Fig. 2 presents similar BTC information for different concentrations of $CaCl_2$ solutions and the two NP sizes at 1 m/day pore water velocity. Fig. 3 shows measured and simulated BTCs for the two NP sizes at various flow velocities ranging from 1 to 20 m/day when the IS was 50 mM NaCl. Fig. 4 presents similar BTC information for the two NP sizes at different velocities, but for 2 mM $CaCl_2$. The BTCs are plotted herein as normalized effluent concentrations (C/C_0) versus the number of pore volumes that passed through the column. Table 2 summarizes the fitted model parameters, along with their 95% confidence intervals. The fitted deposition parameters were found to be unique, as the final fitted values were not affected by the initial guess.

In general, the BTCs were initially delayed (arriving after 1 pore volume), next they rapidly increased, and then they slowly approached the influent particle concentration. These trends can be explained by considering the simulated kinetics of the deposition process using Eqs. (1)–(3). The one-site kinetic model incorporating the Langmurian or RSA blocking function failed to fit the entire BTC obtained at various chemical and physical conditions (data not shown). Conversely, the two-site kinetic model with a Langmurian blocking function for each site provided an excellent description for all the BTCs shown in Figs. 1–4 ($R^2 > 94\%$). In general, the value of k_1 was around one order of magnitude greater than k_2, and S_{max1} was much smaller than S_{max2}. The time delay of the breakthrough curve was mainly determined by the values of k_1 and S_{max1}. A high value of k_1 results in complete deposition until the solid phase concentration of NPs in site 1 approaches S_{max1}. Consequently, more delay is expected for higher values of k_1 and S_{max1}. Other studies on NP transport in porous media have observed a similar delay in their BTCs (e.g., [3,22,32]). After the BTCs begin their sharp rise due to filling of site 1, the shape of the BTCs is mainly controlled by site 2. In particular, the skewness of the rising portions of the BTCs is strongly affected by the values of k_2 and S_{max2}. Neglecting detachment in the model is justified by the negligible tailing in the BTCs.

Two-site kinetic models have previously been employed in colloid and NP transport studies [60–62]. There are a variety of potential explanations for the need to a multiple deposition site model. Macro-scale patch-wise charge heterogeneities have been demonstrated to cause two types of kinetic rates [63]. Primary and secondary minimum interactions may also produce irreversible and reversible deposition sites, respectively [63]. Nanoscale physical and chemical heterogeneity may affect the amount and strength of these primary and secondary minimum interactions [34,64–66]. Differences in the rate and extent of deposition can also occur on flat surfaces, at surface roughness locations, and grain-grain contacts due to changes in the adhesive and hydrodynamics torques [35]. Fig. 5 presents typical SEM images of the NP deposition on

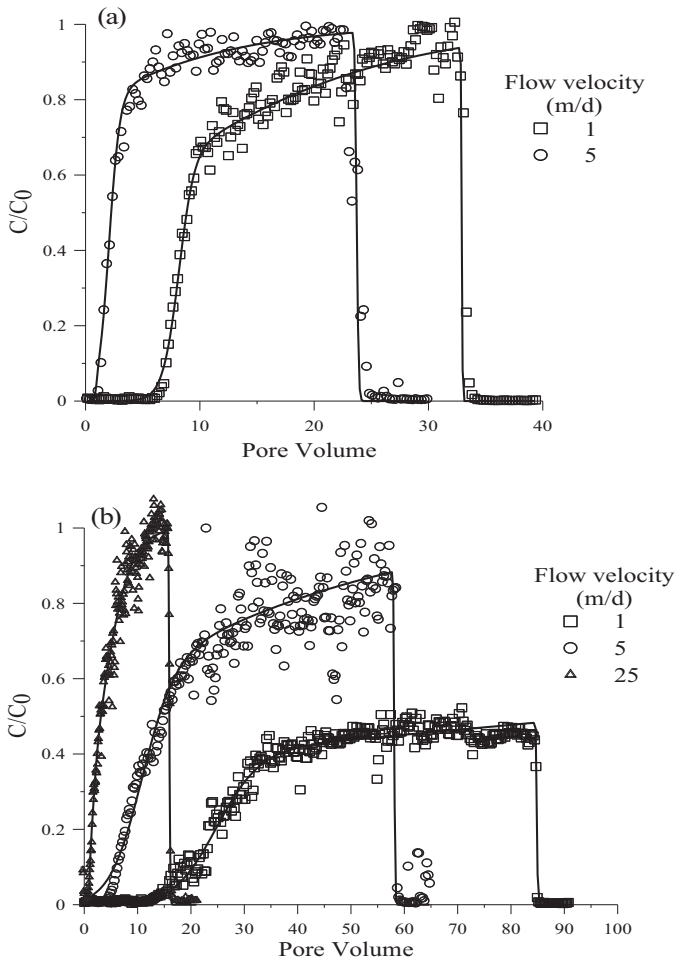

Fig. 4. Representative measured and fitted breakthrough curves for 100 nm (a) and 50 nm (b) modified latex nano-particles obtained from column experiments at 2 mM $CaCl_2$ and various flow velocities. Table 2 provides summary information on the model parameters.

the sand surfaces. SEM images reveal significant surface roughness and irregularities, with depressions and grooves having dimensions much larger in scale than the NPs used in the experiments. Greater amount of NP deposition occurred on microscopically rough than smooth regions on the sand grains in further support of our two-site modeling approach.

Variations of mass transfer rates of NPs to deposition sites on sand grains may also contribute to the need for a model with multiple deposition sites. Colloid filtration theory (CFT) predicts that aqueous phase mass transfer of colloidal particles to the collector surface occurs by Brownian diffusion, interception, and sedimentation [47]. In general, the mass transfer rate varies with distance over the collector surface [67]. Brownian diffusion is predicted by CFT to be the dominant process of the aqueous phase mass transfer for the NPs, and it is more uniformly distributed over the collector surface than sedimentation or interception. In addition, variations in the sand surface topography affect the rates of mass transfer to specific locations on a sand grain [35,67]. These spatial variations in mass transfer have less of an influence on the overall deposition rate under clean-bed conditions than when the selected sites are filled.

In addition, CFT does not account for the potential contribution of solid phase mass transfer and the shadow effect on NP deposition kinetics. Experimental and theoretical results indicate that colloids that are weakly associated with the solid surface via a shallow secondary minimum may translate over the solid surface by hydrodynamic forces to regions where deposition is favorable [11,48]; e.g., regions with greater adhesive forces (chemical heterogeneity) or lower hydrodynamic forces (large scale surface roughness or grain–grain contact). Malysa et al. [68] and Ko and Elimelech [37] reported that micro-scale surface roughness or deposited particles can create excluded zones for colloid deposition immediately behind physical barriers. Indeed, Meinders et al. [69] and Van de Ven et al. [70] microscopically studied colloid attachment on glass surfaces in a parallel flow chamber and observed that particle deposition was less probable on areas down gradient of already deposited particles. It is important to recognize that shadow regions can only be filled up by diffusive transport of NPs from the bulk solution, and not by rolling or translating colloids on unfavorable regions of the collector surface. Fig. 6 schematically illustrates a shadow region created down gradient of a surface protrusion due to the combined effects of weak interaction energies on the up-gradient unfavorable regions and hydrodynamic shear forces. It is therefore logical to anticipate that solid phase NP transport will contribute to higher values of k_1 than k_2, and that k_2 will be impacted by the shadow effect.

3.3. The effect of solution chemistry

Inspection of Fig. 1 reveals that the deposition behavior is highly dependent on the NP size and IS. In particular, greater amounts of deposition occurred at a higher IS and for the smaller NP (at a given IS). The BTCs were delayed longer and the rising limb approached unity much slower at a higher IS and for the smaller NP size (50 nm). Consistent with this blocking behavior, Table 2 indicates that S_f increased in a linear manner with IS, and that larger values of S_f were associated with the smaller NP. It is interesting to note that only a small fraction of the solid surface contributed to NP deposition even at the highest IS (60 mM).

These results are in agreement with experimental and theoretical findings that indicate that colloid deposition is highly dependent on the size and amount of nanoscale heterogeneity [64,71,72]. Kozlova and Santore [64] experimentally demonstrated that 0.5 μm silica particles attached to net-negative and net-repulsive substrates on which nano-textured positive patches (11 nm) were randomly distributed. Transport experiments and simulations revealed that negative colloids (500–2000 nm) attached to positive patches on negative surfaces at high IS, but not at low IS [72]. Theoretical calculations further demonstrated that the nano-scale physical and/or chemical heterogeneities exerted a greater effect on interaction energies at higher IS and for smaller colloid sizes, and that the energy barrier can be completely eliminated to produce finite primary minimum interactions depending on the relative size of heterogeneity to the NP, density of heterogeneity, and solution IS [15,66,71,73]. The aforementioned results indicate that the size and density of nanoscale heterogeneity plays a critical role on the amount and rate of NP deposition. It should be noted that negligible deposition of NPs was observed when the solution IS was 1 mM NaCl (data not shown), ruling out the importance of micro- and macro-scale positively charged heterogeneities (e.g., patches of metal oxides on the sand surfaces) on the NP deposition at higher IS.

Fig. 2 exhibits similar trends to Fig. 1 with regard to the effects of IS and NP size. In contrast, greater amounts of deposition occurred in the presence of Ca^{2+} (Fig. 2) than Na^{+} (Fig. 1) at a smaller solution IS. This also produced correspondingly higher values of S_f presented in Table 2. The higher deposition in the presence of Ca^{2+} can be explained by the formation of divalent cation (Ca^{2+}) bridging as described by previous studies [3,74,75]. These studies have reported that complexation of Ca^{2+} ions to the silanol groups on the mineral surfaces and carboxylic acid groups on the surface of the

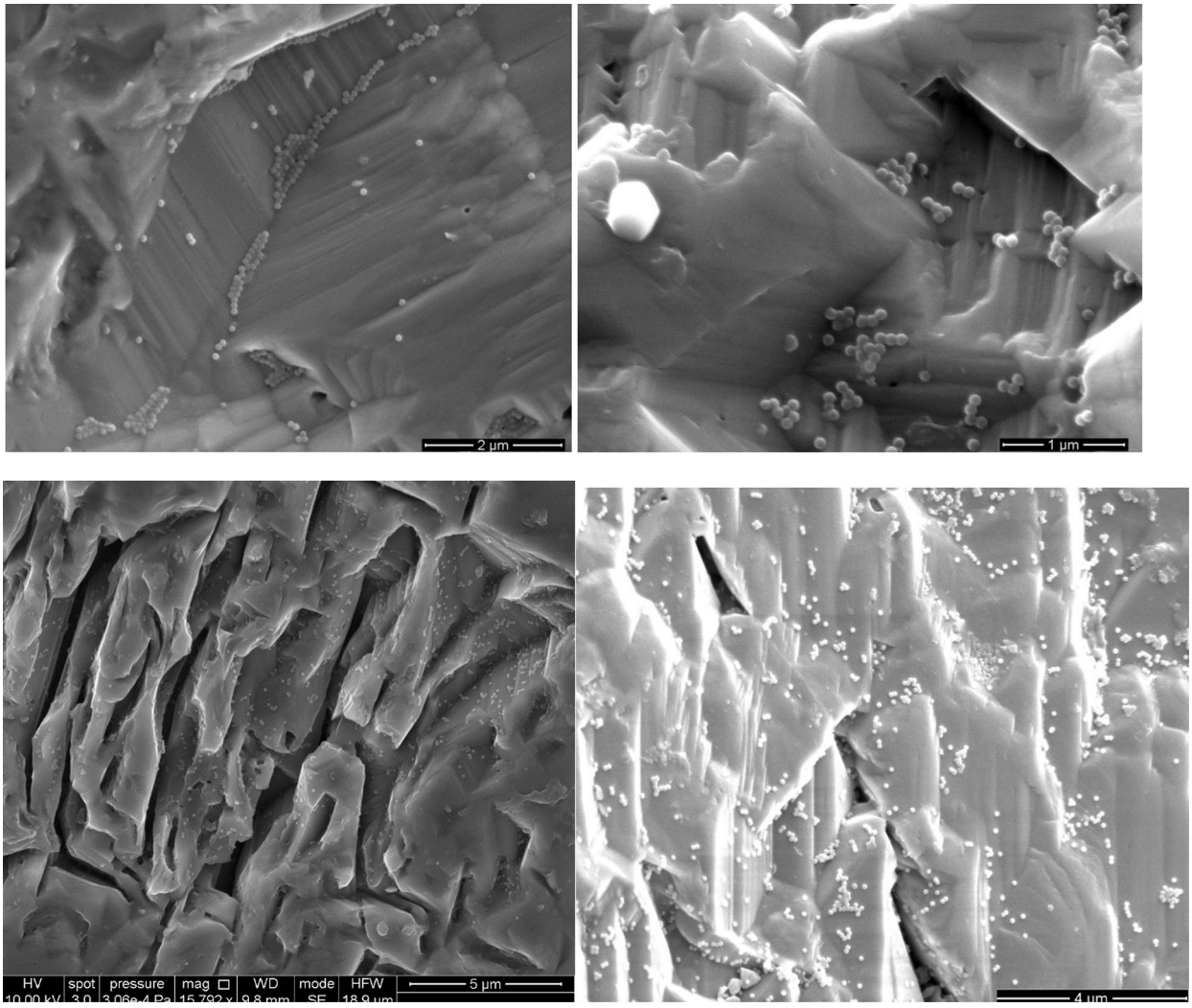

Fig. 5. SEM images showing significant surface roughness and irregularities, with depressions and grooves having dimensions much larger in scale than the NPs. Greater amount of NP (100 nm) deposition occurred on depression and groove regions. SEM images were performed for a few sand grains randomly taken from the column at 50 mM NaCl and flow velocity of 1 m/day following the completion of the deposition experiment in which the effluent NP concentration reached the influent concentration implying that all the deposition sites were filled up.

NPs produces localized nano-scale chemical heterogeneities that are favorable for deposition.

3.4. The effect of flow velocity

Figs. 3 and 4 demonstrate that the delay in the BTCs becomes shorter and NP deposition decreased with increasing flow velocity. Consistent with our observations, CFT predicts that NP deposition decreases with increasing velocity [5]. Table 2 indicates that values of S_f are sensitive to the flow velocity. In particular, higher values of S_f occurred at a lower velocity and for a smaller NP size. These trends may partially be explained by torque balance considerations. In particular, a smaller hydrodynamic torque/force acts on NPs adjacent to the solid surface as the flow velocity decreases and for smaller NP size [40]. To further explore the underlying mechanisms, the flow rate was increased to yield a flow velocity of 100 m/day following the completion of transport experiments at 1 m/day. If the torque balance was the only factor determining S_f, there should be some NP release when the flow velocity was increased to 100 m/day because the higher drag force should be sufficient to overcome the resisting adhesive torque leading to NP release. However, the effluent breakthrough concentrations did not show any NP release when the velocity was increased to 100 m/day. This result indicates the presence of a sizable adhesive torque and/or negligible hydrodynamic torque acting on the deposited NP. Several other explanations have been proposed in the literature for the effect of velocity on NP deposition. These explanations are briefly examined below.

Ko and Elimilech [37] observed that increasing flow velocity decreased S_f at a given IS in packed column experiments. They attributed this observation to larger shadow areas down gradient of deposited particles and protrusions on sand grains. It was postulated that these shadow regions were not accessible for particle deposition at higher velocities. However, diffusive transport is very high for our NPs and particle deposition on regions down gradient of protrusions (shadow areas) should be accessible as quantified by k_2. Therefore, we postulate that the shadow effect or depletion zone only influenced the deposition rates of the NPs and does not affect the values of S_f. Alternatively, assuming that the adhesion strength increases with the residence time can provide a viable explanation for higher S_f values at lower velocities (higher residence time). The adhesion strength of latex particles and bacteria to glass surfaces has been observed to increase with the residence time of the particle on the substrate [76–79]. For example, Xu et al. [78], using colloid probe atomic force microscopy (AFM) observed that the adhesion force between a latex microsphere and glass surfaces increased with residence time over a range of 0.001–50 s. This

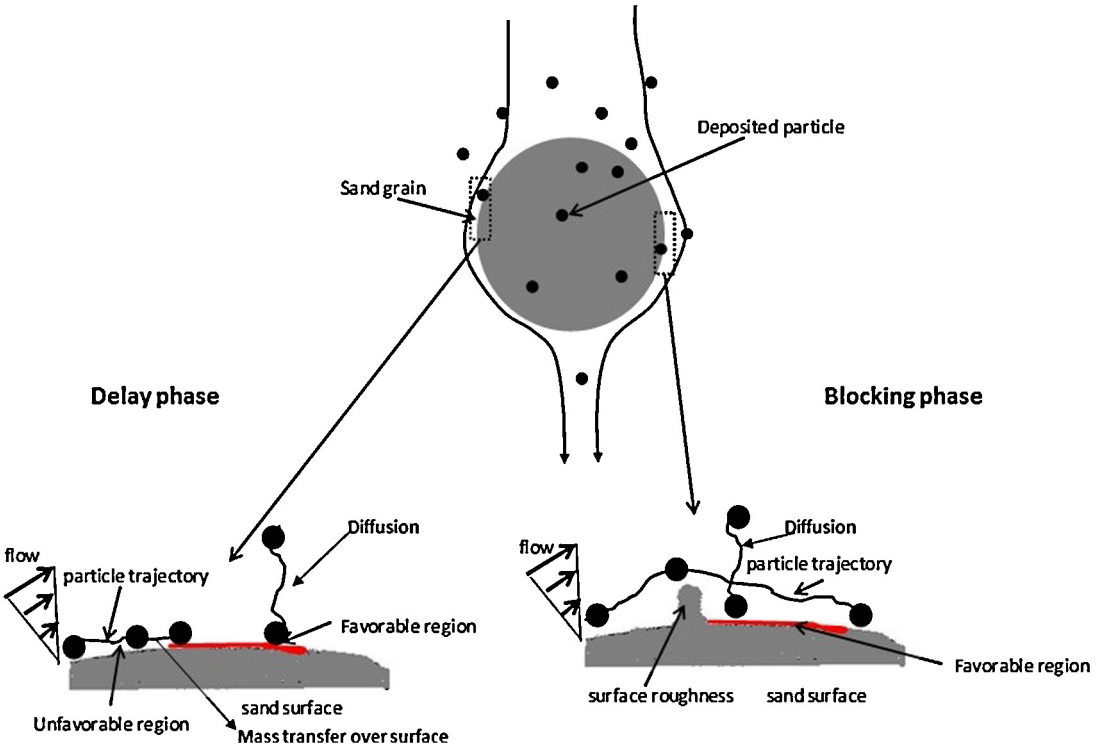

Fig. 6. Schematic of the NP attachment process on a sand grain illustrating the process of mass transfer of NPs over the unfavorable regions and NP attachment on the favorable regions (red area); and a favorable site for attachment located in the "shadow region" down gradient of a surface protrusion. Note that the NPs transferred from the up-gradient unfavorable regions cannot land on the favorable region and NP attachment may only occur due to direct diffusion from the bulk solution. (For interpretation of the references to color in this figure legend, the reader is referred to the web version of the article.)

observation has been ascribed to progressive removal of interfacial water and/or rearrangement of the functional groups on the surface of latex particles to bridge and then bind to the opposing surface until all bonds reach the lowest energy state. Aging of the bond between adhering microorganisms and solid surfaces has been documented [80,81], and attributed to possible collapse of surface appendages, biosurfactant release, and the metabolic activity of the organisms.

4. Conclusions

Spatial and temporal variations in the rate of NP deposition may occur in porous media for a variety of reasons, including: different strengths of interaction energy; enhanced retention in specific locations; spatial variations in NP mass transfer rates to retention locations; and the shadow effect. The influence of multiple rates of deposition may not be apparent on NP BTCs under clean-bed conditions because the retention locations are far from being filled. Conversely, as retention locations are filled, the influence of multiple deposition rates becomes more apparent. Long-term BTCs (25–85 pore volumes) were therefore obtained for (50 and 100 nm) NPs in order to determine their full deposition kinetics under various physicochemical conditions.

The long-term BTCs exhibited a bimodal shape that was successfully simulated using a two-site kinetic model that accounted for irreversible deposition and blocking on each site. Results showed that S_f values (related to the maximum solid concentration of the NPs) were small (<9%) in an acid-washed sand and controlled by the coupled effects of flow velocity, solution chemistry, and particle size; e.g., increasing with decreasing particle size and flow velocity, and increasing IS. NP deposition was much more pronounced in the presence of Ca^{2+} than Na^{+}, implying that NP deposition occurred because of physicochemical interactions between the negatively charged COOH groups on the NPs and nanoscale heterogeneities on the sand surface. Our results suggest these NP interactions tended to strengthen with increasing contact time.

Acknowledgments

Funding for this research was provided by the National Centre for Groundwater Research and Training, an Australian Government initiative, supported by the Australian Research Council and the National Water Commission, and by CSIRO Water for a Healthy Country Flagship research program. The work was conducted in the CSIRO Land and Water Laboratory on the Waite Campus, Adelaide, South Australia.

References

[1] Y. Jin, M. Flury, Fate and transport of viruses in porous media, Adv. Agron. 77 (2002) 39–102.
[2] S.A. Bradford, S. Torkzaban, H. Kim, J. Simunek, Modeling colloid and microorganism transport and release with transients in solution ionic strength, Water Resour. Res. 48 (2012).
[3] S. Torkzaban, J. Wan, T.K. Tokunaga, S.A. Bradford, Impacts of bridging complexation on the transport of surface-modified nanoparticles in saturated sand, J. Contam. Hydrol. 136–137 (2012) 86–95.
[4] A.R. Petosa, D.P. Jaisi, I.R. Quevedo, M. Elimelech, N. Tufenkji, Aggregation and deposition of engineered nanomaterials in aquatic environments: role of physicochemical interactions, Environ. Sci. Technol. 44 (2010) 6532–6549.
[5] J.F. Schijven, S.M. Hassanizadeh, Removal of viruses by soil passage: overview of modeling, processes, and parameters, Crit. Rev. Environ. Sci. Technol. 30 (2000) 49–127.
[6] R. Anders, C.V. Chrysikopoulos, Virus fate and transport during artificial recharge with recycled water, Water Resour. Res. 41 (2005) W10415, http://dx.doi.org/10.1029/2004WR003419.
[7] N. Solovitch, J. Labille, J. Rose, P. Chaurand, D. Borschneck, M.R. Wiesner, J.Y. Bottero, Concurrent aggregation and deposition of TiO_2 nanoparticles in a sandy porous media, Environ. Sci. Technol. 44 (2010) 4897–4902.
[8] D.P. Jaisi, M. Elimelech, Single-walled carbon nanotubes exhibit limited transport in soil columns, Environ. Sci. Technol. 43 (2009) 9161–9166.

[9] A.J. Pelley, N. Tufenkji, Effect of particle size and natural organic matter on the migration of nano- and microscale latex particles in saturated porous media, J. Colloid Interface Sci. 321 (2008) 74–83.
[10] S.A. Bradford, Y. Wang, H. Kim, S. Torkzaban, J. Šimůnek, Modeling microorganism transport and survival in the subsurface, J. Environ. Qual. 43 (2014) 421–440.
[11] S. Torkzaban, Y. Kim, M. Mulvihill, J. Wan, T.K. Tokunaga, Transport and deposition of functionalized CdTe nanoparticles in saturated porous media, J. Contam. Hydrol. 118 (2010) 208–217.
[12] Y. Li, Y. Wang, K.D. Pennell, L.M.A. Briola, Investigation of the transport and deposition of fullerene (C60) nanoparticles in quartz sands under varying flow conditions, Environ. Sci. Technol. 42 (2008) 7174–7180.
[13] J. Virkutyte, S.R. Al-Abed, H. Choi, C. Bennett-Stamper, Distinct structural behavior and transport of TiO_2 nano- and nanostructured particles in sand, Colloids Surf. A 443 (2014) 188–194.
[14] Z. Adamczyk, A. Bratek, E. Szelag, A. Bastrzyk, A. Michna, J. Barbasz, Colloid particle deposition on heterogeneous surfaces produced by polyelectrolyte adsorption, Colloids Surf. A 343 (2009) 111–117.
[15] S.A. Bradford, S. Torkzaban, Colloid interaction energies for physically and chemically heterogeneous porous media, Langmuir 29 (2013) 3668–3676.
[16] Y. Wang, Y. Li, J.D. Fortner, J.B. Hughes, L.M. Abriola, K.D. Pennell, Transport and retention of nanoscale C60 aggregates in water-saturated porous media, Environ. Sci. Technol. 42 (2008) 3588–3594.
[17] J. Shang, C. Liu, Z. Wang, Transport and retention of engineered nanoporous particles in porous media: effects of concentration and flow dynamics, Colloids Surf. A 417 (2013) 89–98.
[18] Y. Jin, Y. Chu, Y. Li, Virus removal and transport in saturated and unsaturated sand columns, J. Contam. Hydrol. 43 (2000) 111–128.
[19] S. Torkzaban, S.A. Bradford, J. Wan, T. Tokunaga, A. Masoudih, Release of quantum dot nanoparticles in porous media: role of cation exchange and aging time, Environ. Sci. Technol. 47 (2013) 11528–11536.
[20] C. Shen, L.-P. Wang, B. Li, Y. Huang, Y. Jin, Role of surface roughness in chemical detachment of colloids deposited at primary energy minima, Vadose Zone J. 11 (2012).
[21] C. Shen, B. Li, Y. Huang, Y. Jin, Kinetics of coupled primary- and secondary-minimum deposition of colloids under unfavorable chemical conditions, Environ. Sci. Technol. 41 (2007) 6976–6982.
[22] Y. Liang, S.A. Bradford, J. Simunek, M. Heggen, H. Vereecken, E. Klumpp, Retention and remobilization of stabilized silver nanoparticles in an undisturbed loamy sand soil, Environ. Sci. Technol. 47 (2013) 12229–12237.
[23] Z. Adamczyk, M. Nattich-Rak, M. Sadowska, A. Michna, K. Szczepaniak, Mechanisms of nanoparticle and bioparticle deposition – kinetic aspects, Colloids Surf. A 439 (2013) 3–22.
[24] Z. Adamczyk, B. Siwek, M. Zembala, P. Belouschek, Kinetics of localized adsorption of colloid particles, Adv. Colloid Interface Sci. 48 (1994) 151–280.
[25] P.R. Johnson, M. Elimelech, Dynamics of colloid deposition in porous media: blocking based on random sequential adsorption, Langmuir 11 (1995) 801–812.
[26] J. Talbot, P. Schaaf, Random sequential adsorption of mixtures, Phys. Rev. A 40 (1989) 422–427.
[27] Z. Adamczyk, B. Siwek, E. Musiał, Latex particle adsorption at heterogeneous surfaces, Colloids Surf. A 214 (2003) 219–229.
[28] M.T.J. van Loenhout, E. Stefan Kooij, H. Wormeester, B. Poelsema, Hydrodynamic flow induced anisotropy in colloid adsorption, Colloids Surf. A 342 (2009) 46–52.
[29] A. Massoudieh, N. Lu, X. Liang, T.H. Nguyen, T.R. Ginn, Bayesian process-identification in bacteria transport in porous media, J. Contam. Hydrol. 153 (2013) 78–91.
[30] S.A. Bradford, S. Torkzaban, J. Simunek, Modeling colloid transport and retention in saturated porous media under unfavorable attachment conditions, Water Resour. Res. 47 (2011).
[31] S.S. Tazehkand, S. Torkzaban, S.A. Bradford, S.L. Walker, Cell preparation methods influence *Escherichia coli* D21g surface chemistry and transport in saturated sand, J. Environ. Qual. 37 (2008) 2108–2115.
[32] I.R. Quevedo, N. Tufenkji, Influence of solution chemistry on the deposition and detachment kinetics of a CdTe quantum dot examined using a quartz crystal microbalance, Environ. Sci. Technol. 43 (2009) 3176–3182.
[33] C. Shani, N. Weisbrod, A. Yakirevich, Colloid transport through saturated sand columns: influence of physical and chemical surface properties on deposition, Colloids Surf. A 316 (2008) 142–150.
[34] S. Torkzaban, S.A. Bradford, M.T. van Genuchten, S.L. Walker, Colloid transport in unsaturated porous media: the role of water content and ionic strength on particle straining, J. Contam. Hydrol. 96 (2008) 113–127.
[35] S. Kalasin, S. Martwiset, E. Bryan Coughlin, M.M. Santore, Particle capture via discrete binding elements: systematic variations in binding energy for randomly distributed nanoscale surface features, Langmuir 26 (2010) 16865–16870.
[36] T. Rizwan, S. Bhattacharjee, Particle deposition onto charge-heterogeneous substrates, Langmuir 25 (2009) 4907–4918.
[37] C.H. Ko, M. Elimelech, The 'shadow effect' in colloid transport and deposition dynamics in granular porous media: measurements and mechanisms, Environ. Sci. Technol. 34 (2000) 3681–3689.
[38] L. Song, M. Elimelech, Calculation of particle deposition rate under unfavourable particle–surface interactions, J. Chem. Soc. Faraday Trans. 89 (1993) 3443–3452.
[39] S. Torkzaban, S.A. Bradford, S.L. Walker, Resolving the coupled effects of hydrodynamics and DLVO forces on colloid attachment in porous media, Langmuir 23 (2007) 9652–9660.
[40] S.A. Bradford, S. Torkzaban, A. Shapiro, A theoretical analysis of colloid attachment and straining in chemically heterogeneous porous media, Langmuir 29 (2013) 6944–6952.
[41] S.A. Bradford, S. Torkzaban, F. Leij, J. Šimůnek, M.T. van Genuchten, Modeling the coupled effects of pore space geometry and velocity on colloid transport and retention, Water Resour. Res. 45 (2009).
[42] A. Kalantariasl, P. Bedrikovetsky, Stabilization of external filter cake by colloidal forces in a well-reservoir system, Ind. Eng. Chem. Res. 53 (2013) 930–944.
[43] P. Bedrikovetsky, F.D. Siqueira, C.A. Furtado, A.L.S. Souza, Modified particle detachment model for colloidal transport in porous media, Transp. Porous Med. 86 (2011) 353–383.
[44] N. Tufenkji, M. Elimelech, Spatial distributions of Cryptosporidium oocysts in porous media: evidence for dual mode deposition, Environ. Sci. Technol. 39 (2005) 3620–3629.
[45] K.E. Nelson, T.R. Ginn, New collector efficiency equation for colloid filtration in both natural and engineered flow conditions, Water Resour. Res. 47 (2011).
[46] H. Yuan, A.A. Shapiro, A mathematical model for non-monotonic deposition profiles in deep bed filtration systems, Chem. Eng. J. 166 (2011) 105–115.
[47] K.-M. Yao, M.T. Habibian, C.R. O'Melia, Water and waste water filtration. Concepts and applications, Environ. Sci. Technol. 5 (1971) 1105–1112.
[48] Z.A. Kuznar, M. Elimelech, Direct microscopic observation of particle deposition in porous media: role of the secondary energy minimum, Colloids Surf. A 294 (2007) 156–162.
[49] M. Elimelech, Effect of particle size on the kinetics of particle deposition under attractive double layer interactions, J. Colloid Interface Sci. 164 (1994) 190–199.
[50] B.V. Derjaguin, L. Landau, Theory of the stability of stongly charged lyophobic sols and the adhesion of strongly charged particles in solution of electrolytes, Acta Physiochim. URS (1941) 633–662.
[51] E.J.W. Verwey, Theory of the stability of lyophobic colloids, J. Phys. Colloid Chem. 51 (1947) 631–636.
[52] J. Gregory, A.J. Wishart, Deposition of latex particles on alumina fibers, Colloids Surf. 1 (1980) 313–334.
[53] J. Bergendahl, D. Grasso, Prediction of colloid detachment in a model porous media: thermodynamics, AIChE J. 45 (1999) 475–484.
[54] J. Gregory, Interaction of unequal double layers at constant charge, J. Colloid Interface Sci. 51 (1975) 44–51.
[55] J. Simunek, M.Th. van Genuchten, M. Sejna, The HYDRUS-1D software package for simulating the one-dimensional movement of water, heat, and multiple solutes in variably-saturated media – version 3.0, HYDRUS software series 1, Department of Environmental Sciences, University of California Riverside, Riverside, CA, 2005, pp. 240 pp.
[56] H.N. Kim, S.A. Bradford, S.L. Walker, *Escherichia coli* O157:H7 transport in saturated porous media: role of solution chemistry and surface macromolecules, Environ. Sci. Technol. 43 (2009) 4340–4347.
[57] J.N. Israelachvili, Intermolecular and Surface Forces, Academic Press, London; San Diego, 1991.
[58] S.A. Bradford, S. Torkzaban, A. Wiegmann, Pore-scale simulations to determine the applied hydrodynamic torque and colloid immobilization, Vadose Zone J. 10 (2011) 252.
[59] E.M.V. Hoek, G.K. Agarwal, Extended DLVO interactions between spherical particles and rough surfaces, J. Colloid Interface Sci. 298 (2006) 50–58.
[60] B. Harmand, E. Rodier, M. Sardin, J. Dodds, Transport and capture of submicron particles in a natural sand: short column experiments and a linear model, Colloids Surf. A: Physicochem. Eng. Aspects 107 (1996) 233–244.
[61] R.C. Bales, S.R. Hinkle, T.W. Kroeger, K. Stocking, C.P. Gerba, Bacteriophage adsorption during transport through porous media: chemical perturbations and reversibility, Environ. Sci. Technol. 25 (1991) 2088–2095.
[62] J.F. Schijven, S.M. Hassanizadeh, R.H.A.M. De Bruin, Two-site kinetic modeling of bacteriophages transport through columns of saturated dune sand, J. Contam. Hydrol. 57 (2002) 259–279.
[63] N. Tufenkji, M. Elimelech, Breakdown of colloid filtration theory: role of the secondary energy minimum and surface charge heterogeneities, Langmuir 21 (2005) 841–852.
[64] M.M. Santore, N. Kozlova, Micrometer scale adhesion on nanometer-scale patchy surfaces: adhesion rates, adhesion thresholds, and curvature-based selectivity, Langmuir 23 (2007) 4782–4791.
[65] R.D. Duffadar, J.M. Davis, Interaction of micrometer-scale particles with nanotextured surfaces in shear flow, J. Colloid Interface Sci. 308 (2007) 20–29.
[66] S.A. Bradford, S. Torkzaban, Colloid adhesive parameters for chemically heterogeneous porous media, Langmuir 28 (2012) 13643–13651.
[67] R. Chatterjee, S.K. Mitra, S. Bhattacharjee, Particle deposition onto Janus and patchy spherical collectors, Langmuir 27 (2011) 8787–8797.
[68] K. Malysa, T. Dabros, T.G.M. Van De Ven, The sedimentation of one sphere past a second attached to a wall, J. Fluid Mech. 162 (1986) 157–170.
[69] J.M. Meinders, J. Noordmans, H.J. Busscher, Simultaneous monitoring of the adsorption and desorption of colloidal particles during deposition in a parallel plate flow chamber, J. Colloid Interface Sci. 152 (1992) 265–280.
[70] T.G.M. van de Ven, P. Warszynski, X. Wu, T. Dabros, Colloidal particle scattering. A new method to measure surface forces, Langmuir 10 (1994) 3046–3056.
[71] R.D. Duffadar, J.M. Davis, Dynamic adhesion behavior of micrometer-scale particles flowing over patchy surfaces with nanoscale electrostatic heterogeneity, J. Colloid Interface Sci. 326 (2008) 18–27.

[72] R. Duffadar, S. Kalasin, J.M. Davis, M.M. Santore, The impact of nanoscale chemical features on micron-scale adhesion: crossover from heterogeneity-dominated to mean-field behavior, J. Colloid Interface Sci. 337 (2009) 396–407.
[73] M. Bendersky, J.M. Davis, DLVO interaction of colloidal particles with topographically and chemically heterogeneous surfaces, J. Colloid Interface Sci. 353 (2011) 87–97.
[74] D. Janjaroen, Y. Liu, M.S. Kuhlenschmidt, T.B. Kuhlenschmidt, T.H. Nguyen, Role of divalent cations on deposition of *Cryptosporidium parvum* oocysts on natural organic matter surfaces, Environ. Sci. Technol. 44 (2010) 4519–4524.
[75] S.B. Roy, D.A. Dzombak, Na^{+}–Ca^{2+} exchange effects in the detachment of latex colloids deposited in glass bead porous media, Colloids Surf. A 119 (1996) 133–139.
[76] T. Dabroś, T.G.M. van de Ven, A direct method for studying particle deposition onto solid surfaces, Colloid Polym. Sci. 261 (1983) 694–707.
[77] J.M. Meinders, H.J. Busscher, Influence of ionic strength and shear rate on the desorption of polystyrene particles from a glass collector as studied in a parallel-plate flow chamber, Colloids Surf. A 80 (1993) 279–285.
[78] L.C. Xu, V. Vadillo-Rodriguez, B.E. Logan, Residence time, loading force, pH, and ionic strength affect adhesion forces between colloids and biopolymer-coated surfaces, Langmuir 21 (2005) 7491–7500.
[79] L.C. Xu, B.E. Logan, Adhesion forces between functionalized latex microspheres and protein-coated surfaces evaluated using colloid probe atomic force microscopy, Colloids Surf. B: Biointerfaces 48 (2006) 84–94.
[80] K.M. Wiencek, M. Fletcher, Bacterial adhesion to hydroxyl- and methyl-terminated alkanethiol self-assembled monolayers, J. Bacteriol. 177 (1995) 1959–1966.
[81] J.M. Meinders, H.C. van der Mei, H.J. Busscher, Deposition efficiency and reversibility of bacterial adhesion under flow, J. Colloid Interface Sci. 176 (1995) 329–341.